Transformation of Surface Roughness of Mg Alloy Tubes During Laser Dieless Drawing

Andrij Milenin, Tsuyoshi Furushima, and Jiří Němeček

The paper investigates the transformation of surface roughness of tubes made from magnesium and magnesium alloys as a function of their longitudinal strain during laser dieless drawing. Experimental studies on three materials (AZ31, MgCa08, and pure Mg) have shown that the dependence of roughness on the longitudinal strain is nonlinear and exhibits a minimum. The proposed explanation for this is that the transformation of surface roughness occurs following two mechanisms. The first mechanism involves stretching of the tube and the decreasing of existing roughness with the increasing elongation. The second mechanism is based on the strain-induced surface roughening phenomenon. This mechanism leads to an increase in roughness with the increasing elongation. To analyze these mechanisms, a numerical model of roughness formation is used. It is experimentally shown that the position of the minimum roughness concerning the tube longitudinal strain is correlated with the stress-strain curve of the material under laser dieless drawing conditions. The obtained results provide a practical way to reduce surface roughness of tubes produced by the laser dieless drawing process. According to the proposed method, to achieve minimum roughness, it is necessary to keep the longitudinal strain under a specific value. This value is close to the strain, which corresponds to the maximum stress on the stress-strain curve of the material for temperature and strain rate, corresponding laser dieless drawing conditions.

1. Introduction

The process of dieless drawing consists of local heating of the material to the temperature of hot deformation with simultaneously controlled stretching. During stretching, the heating zone moves along the length of the workpiece and stretching appears along the entire length of the sample (except the fixing points). Weiss and Kot proposed this process in 1969 (Ref 1) for the elongation of a wire. The dominant features of this process are the absence of a deforming die and lubrication, which lowers the production costs. The dieless drawing was used by Sekiguchi et al. (Ref 2) for the deformation of bars. They noticed another advantage of this method—the absence of friction. This simplifies the processing of materials with low workability. Extending this idea, Furushima and Manabe (Ref 3) applied a dieless drawing to the elongation of microtubes in superplastic conditions for AZ31 and Zn-Al alloys. Kustra et al. (Ref 4) demonstrated that the dieless drawing process allows achieving a significant elongation of the workpiece in one pass (up to 60%) for MgCa08 magnesium alloy with increased biocompatibility. Supriadi et al. (Ref 5) showed that the dieless

drawing allows obtaining products with a variable cross section along the product length. During conventional dieless drawing, electric or induction methods of heating are used. Li et al. (Ref 6) proposed the laser dieless drawing method, where heating was performed by a laser beam. The laser dieless drawing method allows for a more accurate and quick temperature control. Moreover, the staying time of the material at a high temperature is significantly reduced compared to other dieless drawing methods. This is because the laser beam heats the material pointwise. This should lead to an improved surface quality by reducing oxidation. This is important both for industrial applications and for the use of magnesium alloy tubes in medicine. However, several problems limit the possibilities of laser drawing technology. Furushima et al. (Ref 7) showed that the main disadvantages of the laser dieless drawing are related to the free deformation of the material, which makes it difficult to obtain expected geometric dimensions. To solve this problem, the calculation of the production parameters based on the three–dimensional finite-element model of the laser dieless drawing process was proposed by Milenin et al. (Ref 8). Milenin (Ref 9) investigated the factors affecting the instability of the diameter of the tubes after the laser dieless drawing. It is shown that the instability of dimensions during the laser dieless drawing has a common mechanism with the appearance of a neck in uniaxial tension. To avoid this problem, the deformation of the material under conditions that correspond to intensive strain hardening can be used.

Another important drawback of the laser dieless drawing method is the lack of control over surface roughness. Furushima et al. (Ref 10) showed that surface roughness causes localization of the strain and predetermines the position of the fracture of the material during further deformation. This shows that the problems of the instability of the diameter and the increase in surface roughness of products during the laser dieless drawing are related. In the conventional drawing,

Andrij Milenin, AGH University of Science and Technology, al. Mickiewicza 30, Kraków 30-059, Poland; **Tsuyoshi Furushima**, University of Tokyo, Komaba 4-6-1, Meguro, Tokyo 153-8505, Japan; and **Jiří Němeček**, Faculty of Civil Engineering, Czech Technical University in Prague, Thákurova 7, Prague 6, Czech Republic. Contact e-mails: milenin@agh.edu.pl, tsuyoful@iis.u-tokyo.ac.jp, and jiri.nemecek@fsv.cvut.cz.

surface roughness of the material is determined by the quality of the die surface. However, during the dieless drawing, geometric dimensions are formed when the material is deformed freely. In this case, the overall roughness can increase due to the effect of strain-induced surface roughening. This phenomenon was well studied for various materials (mainly for sheets and for cold deformation), for example for steel (Ref 11), aluminum alloys (Ref 12), or titanium (Ref 13). The strain-induced surface roughening is caused by the uneven distribution of mechanical properties in the material which may be a consequence of the crystallographic texture, the presence of inclusions, or the multiphase composition of the material. Dai and Chiang (Ref 14) experimentally studied the mechanism of plastic strain-induced surface roughness. They concluded that roughness is proportional to the amount of plastic strain and the average grain size. Stoudt et al. (Ref 15) experimentally investigated the relationship between strain-induced surface roughness and plastic strain at room temperature on samples with initial roughening. They obtained a monotonic increase in roughness with the increasing strain, regardless of the initial roughness. Knysh et al. (Ref 16) showed that strain-induced surface roughening increases monotonically with the increasing elongation (only cold deformation is considered). Crystal plasticity was used as a basis of numerical modeling of this phenomenon. This allowed the authors to take into consideration the crystallographic texture. However, the possibility of inclusion of other phases is not taken into consideration in this solution. Additionally, crystal plasticity modeling is complex, the computational cost is high, and the calibration of the model for hot deformation is difficult. For these reasons, Furushima et al. (Ref 17) used an isotropic FEM model with mesoscopic material inhomogeneity caused by different flow stress for each crystal grain for strain-induced roughness prediction. The experimental results of this study are in good agreement with the FEM simulation results.

Together, the presented studies indicate the following problems of the laser dieless drawing, associated with surface roughness of processed materials.

- When using the laser dieless drawing, the increase in roughness becomes a factor limiting the capabilities of this technology. Increase in roughness negatively affects the surface quality and reduces the workability of the material. The cause of the increase in roughness is the well-known strain-induced roughness phenomenon.
- The existing studies on strain-induced roughness considers cold deformation only, whereas hot deformation of the material takes place in the process of the laser dieless drawing. At the same time, existing strains in the laser dieless drawing process are in the range of 0-0.6, which significantly exceeds the range of strain studied in the existing works.
- There are no experimental data on the effect of the rheological properties (flow stress model) of the material on the formation of roughness. With hot deformation, much more complex dependence of the flow stress on the strain, temperature, and strain rate is observed than for cold deformation. On the other hand, it is known that the rheological properties of the material affect diameter heterogeneity of the product during the laser drawing. For this reason, it can be assumed that in a similar way this factor affects roughness.

The problem of variable surface roughness also has an important practical aspect in the case of tube production by the laser dieless drawing. Roughness affects the rate of corrosion, wear, and adhesion of substances to the tube walls.

Thus, this paper is devoted to experimental studies of the dependence of surface roughness on the longitudinal strain and the rheological properties of the material during the laser dieless drawing.

2. Materials

2.1 Initial Materials

Extruded tubes with an external diameter of 5.5 mm and an internal diameter of 4.0 mm were used as initial workpieces for the laser dieless drawing (Ref 18). Tubes were prepared from three materials: pure magnesium (99.9 wt.%), MgCa0.8 (0.8 wt.% Ca, Mg balanced), and AZ31 (3 wt.% Al, 1 wt.% Zn, Mg balanced). The MgCa0.8 alloy is selected as an example of a material used in medicine (Ref 19). AZ31 alloy is one of the most popular in the industry. This alloy is well studied in existing works. Pure magnesium is used as a reference material.

2.2 Experimental Study of the Flow Stress

The flow stress measurement for Mg and MgCa0.8 alloy was performed on a test machine ZWICK 250. The initial dimensions of the samples for these tests are 8 mm in diameter and 10 mm in height. The temperature range was 20-400 °C, and the strain rate interval 0.01-1.0 s^{-1}. To eliminate the effect of friction, a graphite-based lubricant was used. The deforming element was heated together with the sample to the same temperature, which eliminated the influence of heat exchange between the sample and the instrument on the results. Experimental data for the AZ31 alloy are taken from the literature (Ref 20). The experimental results were approximated by the following equation, proposed by Hensel and Spittel (Ref 21):

$$\sigma = m_1 \exp(m_2 t)\varepsilon^{m_3}\dot{\varepsilon}^{m_4}\exp\left(\frac{m_5}{\varepsilon}\right)(1+\varepsilon)^{m_6 t}\exp(m_7\varepsilon)\dot{\varepsilon}^{m_8 t}t^{m_9}$$

(Eq 1)

where σ is the flow stress, t is the temperature, ε is the strain, $\dot{\varepsilon}$ is the strain rate, and m_{1-9} are material constants.

The values of the empirical coefficients m_i for the three materials found as the best fit are provided in Table 1. The empirical coefficients for AZ31 alloy were determined based on the experimental data presented by Kuc and Pietrzyk (Ref 20) for strain rates 0.1 s^{-1} and 0.01 s^{-1}.

The comparison of stress-strain curves for conditions close to the laser dieless drawing conditions (temperature 250-400 °C and strain rate 0.01-0.1 s^{-1}) is shown in Fig. 1. All obtained curves have a maximum in the range of strains, which is typical for the laser dieless drawing process (0-0.6). This maximum is less noticeable for pure magnesium and more noticeable for the AZ31 alloy. As follows from the experimental stress-strain curves in Fig. 1, their shape and position of the maximum of stress do not change with the change in the strain rate and varies slightly with the change in temperature. The greatest effect of temperature on the strain, which corresponds to the maximum stress, is observed for the MgCa0.8 alloy. For this alloy, the position of the maximum stress corresponds to a strain of 0.35 at 250 °C and a strain of 0.1 at 350 °C. The most stable position of the maximum stress is for pure magnesium (strain of 0.1) and AZ31 alloy (strain of 0.2).

	m_1	m_2	m_3	m_4	m_5	m_6	m_7	m_8	m_9
AZ31	2517	− 0.007459	0.2200	0.1900	0	0	− 0.9780	0	0
Mg	1133.6	− 0.0005792	− 0.1661	− 0.3498	− 0.01571	− 0.0003246	0.1166	0.001440	− 0.5538
MgCa08	851.4	− 0.004240	0.2844	− 0.4118	− 0.001359	− 0.003966	− 0.03966	0.001778	− 0.02445
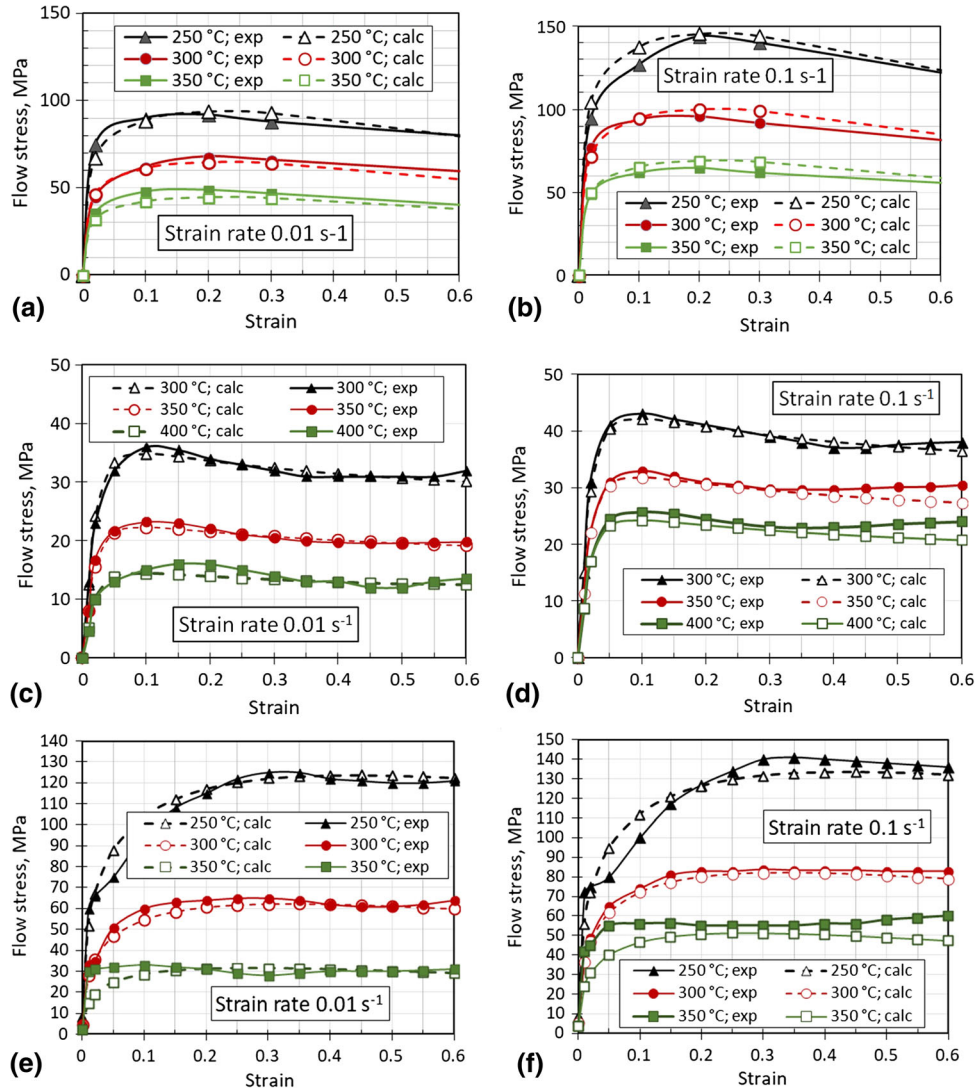
Fig. 1 Dependence of the flow stress on the strain of AZ31 (a, b), Mg (c, d), and MgCa08 (e, f) alloys for strain rates of 0.01 s^{-1} and 0.1 s^{-1} (dotted lines—approximation (1), solid lines—experiment)

3. Experimental Study on Surface Roughness After the Laser Dieless Drawing Process

3.1 The Laser Dieless Drawing Experiment

The laser dieless drawing process (Fig. 2) was applied to the extruded tubes. During the laser drawing, the tube is stretched due to the speed difference V_1-V_2 (Fig. 2a). The rotation of the tube around its axis, shown in Fig. 2(a), allows heating the tube more evenly since the laser beam acts only on one side (position 1 in Fig. 2).

The maximum temperature reached in the deformation zone was 300 °C for all materials. In the process of the laser dieless drawing, the initial velocities were $V_2 = 0.5$ mm/s and $V_1 = 0.5$ mm/s. Then, when the temperature reached 300 °C, the velocity V_1 monotonically increases which increases the elongation of the tube. Thus, during the deformation of each specimen, elongation increased during the experiment. On each sample, several zones with different elongation appeared. The zones and sampling of the tubes are shown in Fig. 3. For each alloy, probe position number 1 corresponds to the undeformed section of the tube. The increasing position number (2, 3, and

4) corresponds to the increasing of the longitudinal strain. Position Nos. 3 or 4 (depending on the total tube length) were always chosen in the most deformed (necking) area. The amount of the longitudinal strain was determined by the measurement of the inner and outer diameters of the tube. For each position, three to four measurements of cross-sectional dimensions were made using a light optical microscope. The longitudinal strain was calculated from the ratio of the current area to position 1 (initial) area and volume constancy condition. The error in determining the longitudinal strain was derived from the error in measuring the dimensions of the tube cross section.

3.2 Experimental Study on Surface Roughness

In this study, no special surface treatment was performed. Samples were gently washed in alcohol and wiped with a soft cloth. Part of the loose oxides was removed (hand washed). Oxides sticking to the surface were not removed by any abrasive or chemical procedure. Standard ISO 4287:1997 surface roughness characteristics (maximum profile valley depth R_y, the difference between the maximum height and the minimum height R_z, arithmetic mean roughness R_a, root-mean-square roughness R_q) were calculated from the contour heights. The R_a roughness is defined as

$$R_a = \frac{1}{n} \sum_{i=1}^{n} |y_i| \qquad \text{(Eq 2)}$$

In this formula, it is assumed that the roughness profile has been filtered from the raw profile data and the mean line has been calculated. The roughness profile contains n ordered, equally spaced points along the trace, and y_i is the vertical distance from the mean line to the data point (Ref 22).

Surface roughness, for example, R_a roughness, can be measured at different scales. Roughness measured along a contour length of a few millimeters is called global roughness. If the measurement scale corresponds to several microns, we will use the term local roughness. Note that the global and local AFM roughness characteristics are calculated for very different surface areas (or the contour length), and they are not directly comparable. In general, the smaller the scanned area, the smaller the roughness characteristics. In other words, each roughness characteristic is related to a corresponding surface area.

Probes from Fig. 3 were analyzed for surface roughness characterized by several means:

1. Global roughness R_a. Side view of the tube was taken in a light optical microscope, and the surface contour was detected and analyzed (ImageJ software). Images were taken in 200x magnification giving the contour length of about 5 mm. The dependence of global roughness R_a on the tube longitudinal strain is shown in Fig. 4.
2. Scanning electron microscope (SEM) imaging. Samples were scanned in a scanning electron microscope (Phenom XL Desktop) equipped with the topographical mode of a back-scattered electron detector, the BSE-topo mode (parameters: 10 kV, 1 Pa, BSE, TopoA, 250x and 500x magnifications), to visualize the surface topography (Fig. 5).
3. Local atomic force microscope (AFM) roughness R_a. The sample surface was scanned by AFM (DS 95, DME Nanotechnologie GmbH) in several arbitrary areas of 25x25 μm in size (Fig. 6), and standard ISO 4287:1997 surface roughness characteristics (R_y, R_z, R_a, R_q) were calculated. The dependence of local AFM roughness R_a on the longitudinal strain is shown in Fig. 7.

3.3 Level of Oxidation

The level of surface oxidation affects the workability during the dieless drawing [see for example (Ref 23)]. In our study, however, the possible effect of oxidation on roughness measurement results is more significant. To eliminate this factor, a study of the level of oxidation was carried out. The vulnerability to oxidation was quantified in a light microscope.
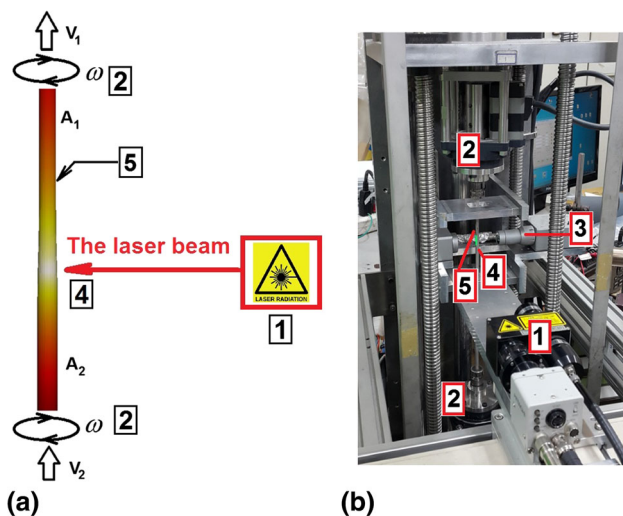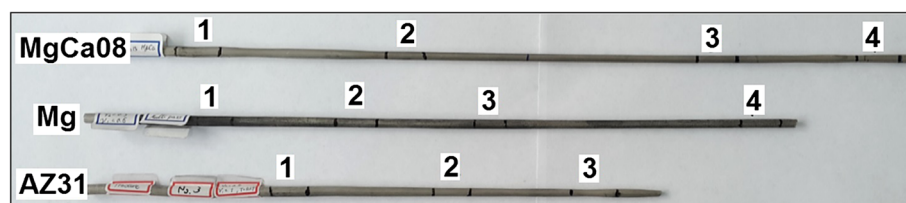

Fig. 2 Principal scheme (a) and example of practical implementation (b) of the laser dieless drawing process (V_1, V_2—stretching velocities, A_1, A_2—tube input and output cross sections, ω—rotation velocity, 1—laser head, 2—rotary stage, 3—diameter measurement device, 4—laser spot, 5—drawn tube)

Fig. 3 Samples after the laser dieless drawing process and numbering of probes positions

An average area covered by oxides on the layer given as a percentage of the whole area had the following values for materials: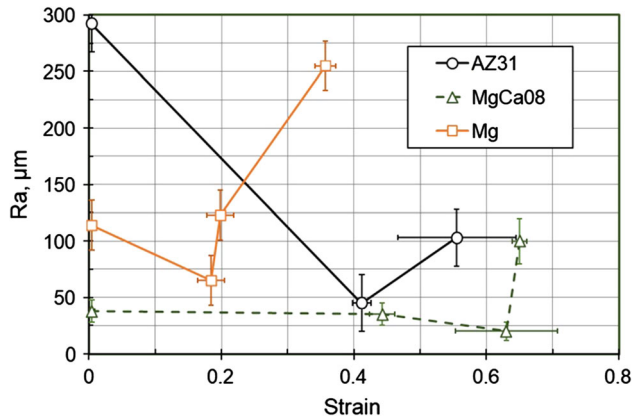 AZ31 $34 \pm 3.6\%$, MgCa0.8 $54 \pm 19\%$, Mg $37 \pm 10\%$. However, a more important result is that the level of surface oxidation does not correlate with the magnitude of the longitudinal strain. In principle, this is the expected result, since all experiments were carried out at the same temperature and speed V_2 (see Fig. 2a).

Fig. 4 Dependence of global roughness R_a on the tube longitudinal strain

4. Discussion

4.1 Experimental Observations

The analysis of experimental studies allows us to make several important observations. It follows from Fig. 4 that the dependence of global roughness R_a on the strain exhibits a minimum. At the initial stage of deformation, roughness decreases. After a specific strain (Mg: 0.18, AZ31: 0.41, MgCa0.8: 0.63), roughness begins to increase. Similar results were obtained for global (Fig. 4) and local AFM roughness (Fig. 7). The strain values corresponding to the minimum roughness are very similar in both cases. For AFM roughness, the specific strain was Mg: 0.20, AZ31: 0.40, MgCa0.8: 0.45.
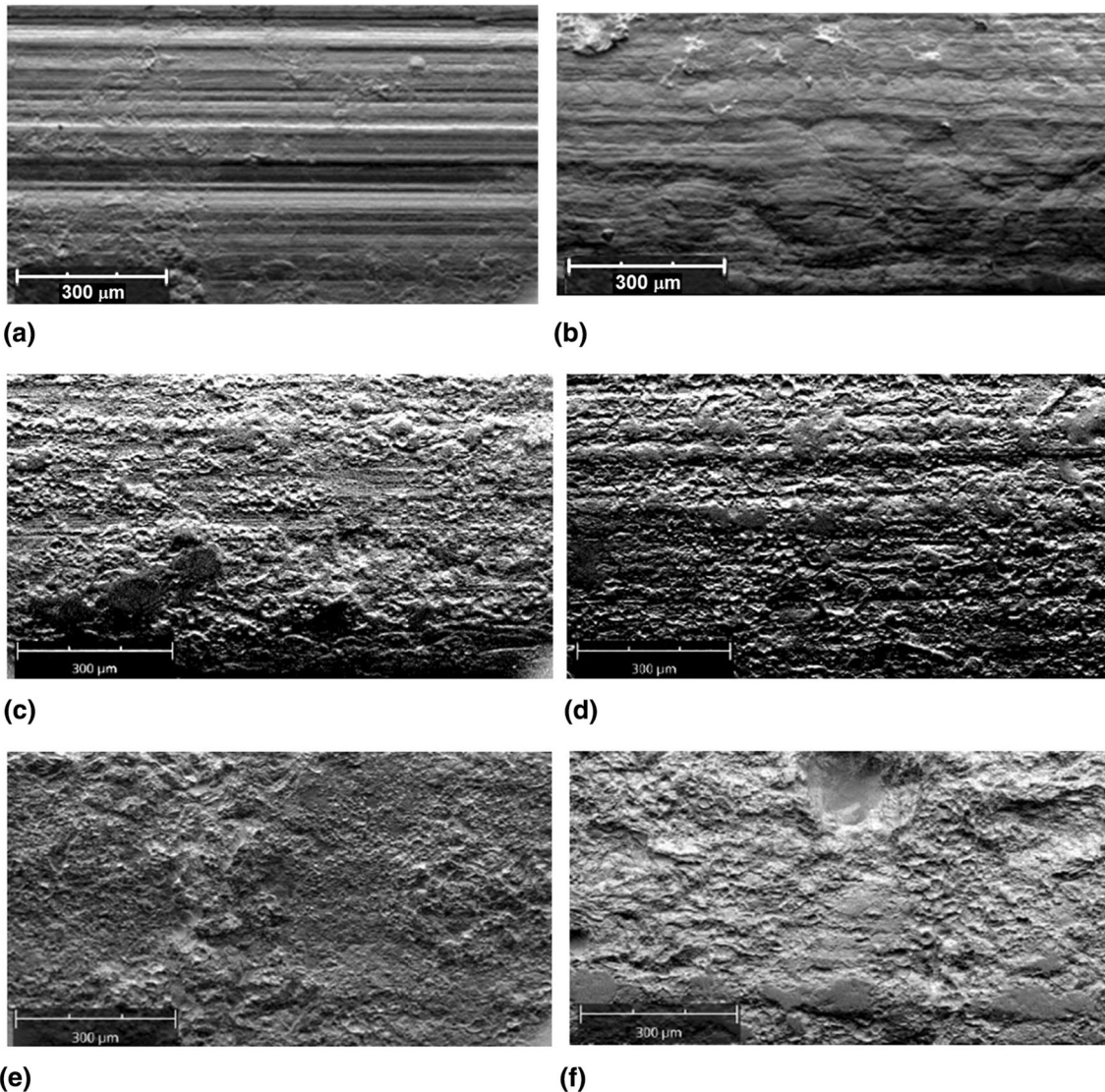

Fig. 5 Examples of SEM images of the surface (a and b—AZ31; c and d—MgCa0.8; e and f—Mg) for the longitudinal strain: (a), (c), (e) 0.0; (b) 0.55; (d) 0.36; (f) 0.65
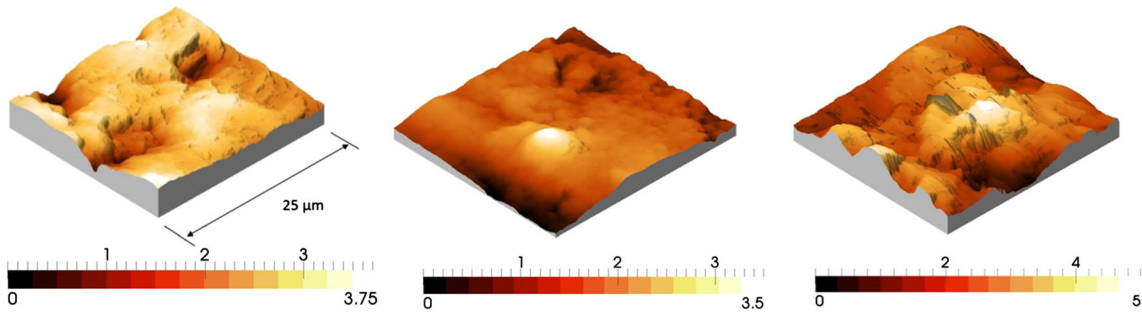
Fig. 6 Example of AFM scan of the initial tube surface measured on 25x25 μm area (left—AZ31, center—MgCa0.8; right—Mg), scales in μm
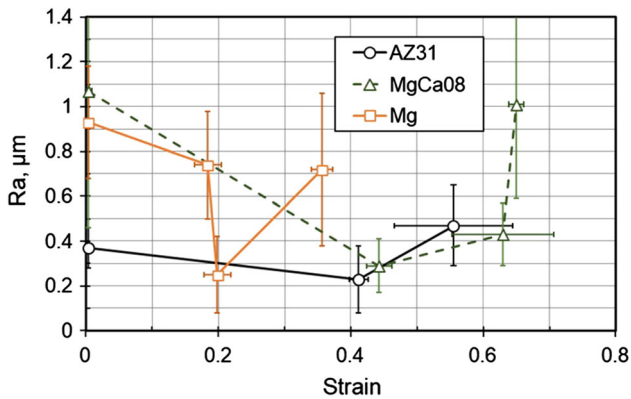

Fig. 7 Dependence of local AFM roughness Ra on the longitudinal strain

Therefore, the observed effect is manifested both in the roughness scale of 50-300 μm (global roughness) and on the scale of 0.2-1.4 μm (AFM roughness).

A comparison of the roughness data with the stress-strain curves allows seeing the following regularity. The strain values corresponding to the maximum stress in stress-strain curves presented in Fig. 1 (Mg: 0.1, AZ31: 0.2, MgCa0.8: 0.3 for temperature 300 °C and strain rate 0.01 s^{-1}) is proportional to the strain that corresponds to the minimum roughness. Thus, it can be justly assumed that the formation of roughness during hot deformation is related to the shape of the stress-strain curve.

The growth of roughness with the increasing strain is apparently caused by the effect of strain-induced roughening. This can be seen also in the surface photographs (Fig. 5b, d, f). The decrease in roughness at the initial stage of stretching is due to the dominance of the effect of material elongation (and the associated decrease in roughness) over the mechanism of strain-induced roughening in later deformation stages. These explanations, however, must be interpreted with caution due to the small number of used samples and materials.

4.2 Explanation of the Observed Effect and Numerical Simulation

The purpose of the numerical simulation was to qualitatively explain the observed patterns of roughness changes depending on the longitudinal strain of the tube. We did not set the goal of a quantitative description of the development of roughness since this task is beyond the scope of this study.

For simulation, we used the two-dimensional numerical model of rigid-plastic deformation of the inhomogeneous microstructure of magnesium alloys. Foundations of the model

are presented in (Ref 24) with a reference to the problem of micro-fractures modeling at grain boundaries of MgCa0.8 alloy during the tensile test. This model uses the multi-domains boundary elements method. It also uses the Kelvin's fundamental solution (Ref 25) as a basis for interpolating increments of displacements and stresses in microstructural grains (domains). The effective flow stress in each grain σ_{eff} was calculated from the following equation:

$$\sigma_{eff} = K_g \sigma(\varepsilon, \dot{\varepsilon}, t) \qquad \text{(Eq 3)}$$

where K_g is a coefficient that takes into consideration the unevenness of effective mechanical properties in different grains; $\sigma(\varepsilon, \dot{\varepsilon}, t)$ is the flow stress (Eq 1).

It is assumed that the unevenness of mechanical properties (value of K_g) is affected by crystallographic texture, the presence of different phases in the material, the presence of dissimilar inclusions. The idea of the influence of the inhomogeneity, associated with the orientations of the grain structure, on the local instabilities of the material flow during deformation was considered, for example, in papers (Ref 26-28). The presence of inclusions and different phases in the AZ31 alloy is discussed in the (Ref 29). The total influence of these factors on the effective grain strength is taken into account by the coefficient K_g.

The values of K_g for all grains of the microstructure model are calculated using an artificial generator with the normal distribution of a random variable. The employed program used the *vdrnggaussian* function included in the Intel® Math Kernel Library. As the parameters of the normal distribution of K_g, the mean value (1.0) and the dispersion (0.076) determined for AZ31 tubes from nanoindentation tests, performed by Jäger et al. (Ref 29), were used. These values are obtained by normalizing the measurement results of the storage module for tubes after extrusion [table 3, line A2 in the (Ref 29)].

For the generation of the initial boundary element domains (grains), the actual microstructure of tubes near the surface was processed according to the algorithm proposed by Rauch and Bzowski (Ref 30). The initial geometry of the relief was approximated by a sinusoid fitted to the AFM initial relief data $R_a = 0.39$ μm (Fig. 7, the curve for AZ31). The steps in generating the domains are shown in Fig. 8.

The results of calculating the average grain strains for a total tube longitudinal strain of 0.001, 0.22, and 0.55 are shown in Fig. 9. As follows from this figure, up to a longitudinal strain value of 0.22 (Fig. 9b), a uniform elongation of the microstructure fragment occurs, which is accompanied by a proportional decrease in the height of the relief. At this stage, the non-uniformity of the deformation caused by the given distribution of is compensated by the strain hardening of the material, and
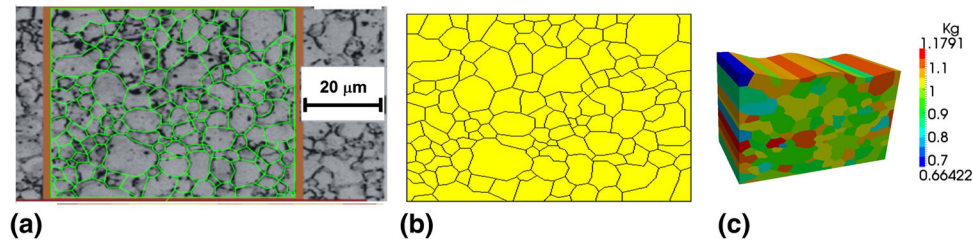
Fig. 8 The steps in generating the boundary element domains from a microstructure of AZ31 tubes after extrusion are as follows: (a) fragment of the microstructure used for its digital representation; (b) digital model of microstructure after image processing; (c) resulting boundary element grid with the distribution of inhomogeneity parameter K_g and artificial roughness
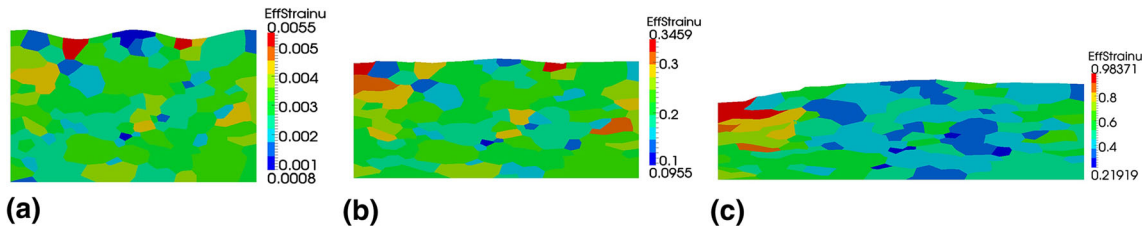

Fig. 9 The effective strains in grains for the fragment of surface roughness of tube from AZ31 alloy: a—total longitudinal strain of tube 0.001; b—0.22; c—0.55

there is no observed localization of the deformation in the form of the strain-induced roughness. This period corresponds to a decrease in roughness in Fig. 4 and 7. With a further increase in the longitudinal strain of the tube, grains appear in the microstructure, the deformation of which is greater than the value corresponding to the maximum on the stress-strain curve (Fig. 1a, b) of AZ31 alloy. As a result, localization of strain in these grains begins, leading to a sharp increase in the strain-induced roughness effect (Fig. 9c). Thus, the transformation of surface roughness during the laser dieless drawing occurs through two mechanisms. The first mechanism involves stretching of the tube and decreasing of existing roughness with the increasing elongation. The second mechanism is based on the strain-induced surface roughening phenomenon. This mechanism leads to an increase in roughness with the increasing elongation.

4.3 Practical Value and Limitations of the Obtained Results

The obtained empirical results will allow minimizing surface roughness of tubes prepared with the laser dieless drawing. To achieve the minimum roughness, it is necessary to keep the longitudinal strain under a critical value. Usually, this value is close to the strain corresponding to the maximum stress in the stress-strain curve of the given alloy for the laser dieless drawing conditions (laser dieless drawing conditions meaning the stress-strain curves should be obtained at a similar temperature and with a similar strain rate).

These conclusions, however, must be interpreted with caution due to a small number of investigated materials and laser dieless drawing conditions. Also, too few samples and materials have been studied. These results do not rule out the influence of other factors on final roughness after the laser dieless drawing, such as initial roughness, microstructure, initial textures. However, even in the presented form, they open up the prospect of improving the quality of the surface of the material after the laser dieless drawing.

5. Conclusions

The presented research aimed to experimentally examine surface roughness formation on tubes made from three materials (AZ31, MgCa0.8, and pure Mg) in the process of the laser dieless drawing. It was established experimentally for the considered magnesium alloys that their surface roughness exhibits a minimum concerning the longitudinal strain of the tube in the laser dieless drawing process. The magnitude of the strain corresponding to the minimum roughness correlated to the strain at which the maximum stress of the stress-strain curve is reached under the laser dieless drawing conditions. Similar results were obtained for global and local AFM roughness.

Results of mathematical modeling and experiments allow concluding that the period of roughness decreasing during tube elongation is related to the processes of material strain hardening. These results, of course, do not rule out the influence of other factors on final roughness.

The obtained results provide a practical direction on how to reduce the surface roughness of tubes produced by the laser dieless drawing process. To achieve the minimum roughness, it is necessary to keep the longitudinal strain under a critical value. Usually, this value is close to the strain, which corresponds to the maximum stress on the stress-strain curve of this alloy under conditions of the laser dieless drawing. These conclusions, however, must be interpreted with caution due to a small number of investigated materials and dieless drawing conditions.

Open Access

This article is licensed under a Creative Commons Attribution 4.0 International License, which permits use, sharing, adaptation, distribution and reproduction in any medium or format, as long as you give appropriate credit to the original author(s) and the source, provide a link to the Creative Commons licence, and indicate if changes were made. The images or other third party material in this article are included in the article's Creative Commons licence, unless indicated otherwise in a credit line to the material. If material is not included in the article's Creative Commons licence and your intended use is not permitted by statutory regulation or exceeds the permitted use, you will need to obtain permission directly from the copyright holder. To view a copy of this licence, visit http://creativecommons.org/licenses/by/4.0/.

References

1. V. Weiss and R.A. Kot, Dieless Wire Drawing with Transformation Plasticity, *Wire J.*, 1969, **9**, p 182–189
2. H. Sekiguchi, K. Kobatake, and K. Osakada, A Fundamental Study on Dieless Drawing, *Machine Tool Design and Research Conference*, S.A. Tobias and F. Koenigsberger, Ed., Palgrave, London, 1975, p 539–544
3. T. Furushima and K. Manabe, Experimental and Numerical Study on Deformation Behavior in Dieless Drawing Process of Superplastic Microtubes, *J. Mater. Process. Technol.*, 2007, **191**, p 59–63
4. P. Kustra, A. Milenin, B. Płonka, and T. Furushima, Production Process of Biocompatible Magnesium Alloy Tubes Using Extrusion and Dieless Drawing Processes, *J. Mater. Eng. Perform.*, 2016, **25**(6), p 2528–2535
5. S. Supriadi, T. Furushima, and K. Manabe, Development of Precision Profile Control System with Fuzzy Model and Correction Function for Tube Dieless Drawing, *J. Solid Mech. Mater. Eng.*, 2011, **5**(12), p 1059–1070
6. Y. Li, N.R. Quick, and A. Kar, Dieless Laser Drawing of Fine Metal Wires, *J. Mater. Proc. Technol.*, 2002, **123**, p 451–458
7. T. Furushima, Y. Imagawa, S. Furusawa, and K. Manabe, Deformation Profile in Rotary Laser Dieless Drawing Process for Metal Microtubes, *Proc. Eng.*, 2014, **81**, p 700–705
8. A. Milenin, P. Kustra, T. Furushima, P. Du, and J. Němeček, Design of the Laser Dieless Drawing Process of Tubes From Magnesium Alloy Using FEM Model, *J. Mater. Proc. Technol.*, 2018, **262**, p 65–74
9. A. Milenin, Rheology-Based Approach of Design the Dieless Drawing Processes, *Arch. Civ. Mech. Eng.*, 2018, **18**(4), p 1309–1317
10. T. Furushima, Y. Imagawa, and K. Manabe, T Sakai Effects of Oxidation and Surface Roughening on Drawing Limit in Dieless Drawing Process of SUS304 Stainless Steel Microtubes, *J. Mater. Proc. Technol.*, 2015, **223**, p 186–192
11. P. Sundaram, Deformation-Induced Surface Roughening Studies in an AISI, 1090 Spheroidized Steel, *Scr. Metallurgica et Materialia*, 1995, **33**(7), p 1093–1099
12. T.J. Turner and M.P. Miller, Modeling the Influence of Material Structure on Deformation Induced Surface Roughening in AA7050 Thick Plate, *J. Eng. Mater. Technol.*, 2007, **129**(3), p 367–379
13. A. Romanova, R.R. Balokhonov, A.V. Panin, E.E. Batukhtina, M.S. Kazachenok, and V.S. Shakhijanov, Micromechanical Model of Deformation-Induced Surface Roughening in Polycrystalline Materials, *Phys. Mesomech.*, 2017, **20**(3), p 324–333
14. Y.Z. Dai and F.-P. Chiang, On the Mechanism of Plastic Deformation Induced Surface Roughness, *J. Eng. Mater. Technol.*, 1992, **114**(4), p 432–438
15. M.R. Stoudt, J.B. Hubbard, and S.D. Leigh, On the Relationship Between Deformation-Induced Surface Roughness and Plastic Strain in AA5052—Is it Really Linear?, *Metallurg. Mater. Trans. A.*, 2011, **42**(9), p 2668–2679
16. P. Knysh, K. Sasaki, T. Furushima, M. Knezevic, and Y.P. Korkolis, Deformation-Induced Surface Roughening of an Al-Mg Alloy, *J. Phys: Conf. Series.*, 2018, **1063**, p 012132
17. T. Furushima, T. Masuda, K. Manabe, and S. Alexandrov, Prediction of Free Surface Roughening by 2D and 3D Model Considering Material Inhomogeneity, *J. Solid Mech. Mater. Eng.*, 2011, **5**(12), p 978–990
18. A. Milenin, P. Kustra, D. Byrska-Wójcik, B. Plonka, V. Petráňová, V. Hrbek, and J. Němeček, Numerical Optimization and Practical Implementation of the Tube Extrusion Process of Mg Alloys with Micromechanical Analysis of the Final Product, *Key Eng. Mater.*, 2016, **716**, p 55–62
19. Z. Li, X. Gu, S. Lou, and Y. Zheng, The Development of Binary Mg-Ca Alloys for Use as Biodegradable Materials Within Bone, *Biomaterials*, 2008, **29**(10), p 1329–1344. https://doi.org/10.1016/j.biomaterials.2007.12.021
20. D. Kuc and M. Pietrzyk, Phisical and Numerical Modelling of Plastic Deformation of Magnesium Alloys, *Comput. Meth. Mater. Sci.*, 2010, **10**(2), p 130–142
21. A. Hensel and T. Spittel, *Kraft - und Arbeitsbedarf bildsamer Formgebungsverfahren*, 1st ed., Deutscher Verlag für Grundstoffindustrie, Leipzig, 1978 (in German)
22. E.P. DeGarmo, J.T. Black, R.A. Kohser, Materials and processes in manufacturing, 9th ed., International ed, Wiley, New York, 2003
23. Y.-M. Hwang and H.-H. Liu, Formability Analysis and Oxidation Layer Effects in Dieless Drawing of Stainless Steel Wires, *Metals*, 2019, **9**(828), p 1–13. https://doi.org/10.3390/met9080828
24. A. Milenin, D.J. Byrska, and O. Grydin, The Multi-Scale Physical and Numerical Modeling of Fracture Phenomena in the MgCa0.8 Alloy, *Comput. Struct.*, 2011, **89**(11–12), p 1038–1049
25. S.L. Crouch and A.M. Starfield, *Boundary Element Methods in Solid Mechanics*, George Allen & Unwin Ltd, London, 1983
26. R. Kulagin, Y. Beygelzimer, A. Mazilkin, and H. Hahn, Modelling of High Pressure Torsion Using FEM, *Proc. Eng.*, 2017, **207**, p 1445–1450
27. N.K. Sundaram, A. Mahato, Y. Guo, K. Viswanathan, and S. Chandrasekar, Folding in Metal Polycrystals: Microstructural Origins and Mechanics, *Acta Mater.*, 2017, **140**, p 67–78
28. R. Kulagin, Y. Beygelzimer, Y. Ivanisenko, A. Mazilkin, B. Straumal, and H. Hahn, Instabilities of Interfaces Between Dissimilar Metals Induced by High Pressure Torsion, *Mater. Lett.*, 2018, **222**, p 172–175
29. A. Jäger, K. Tesař, J. Němeček, A. Milenin, and J. Němeček, Microstructure and Micromechanical Properties of Mg Microtubes Prepared by Laser Dieless Drawing, *Key Eng. Mater.*, 2018, **784**, p 21–26. https://doi.org/10.4028/www.scientific.net/KEM.784.21
30. L. Rauch and K. Bzowski, Image processing methods for segmentation of microscopic pictures of the MgCa alloys, *Comput. Method Mater. Sci.*, 2011, **11**(2), p 350–356